Check for updates

ADVANCED MATERIALS
www.advmat.de

Design of Materials Configuration for Optimizing Redox-Based Resistive Switching Memories

*Shaochuan Chen and Ilia Valov**

Redox-based resistive random access memories (ReRAMs) are based on electrochemical processes of oxidation and reduction within the devices. The selection of materials and material combinations strongly influence the related nanoscale processes, playing a crucial role in resistive switching properties and functionalities. To date, however, comprehensive studies on device design accounting for a combination of factors such as electrodes, electrolytes, and capping layer materials related to their thicknesses and interactions are scarce. In this work, the impact of materials' configuration on interfacial redox reactions in HfO_2-based electrochemical metallization memory (ECM) and valence-change memory (VCM) systems is reported. The redox processes are studied by cyclic voltammetry, and the corresponding resistive switching characteristics are investigated. In ECM cells, the overall cell resistance depends on the electrocatalytic activity of the counter electrode. Nonetheless, the capping layer material further influences the cell resistance and the SET and RESET voltages. In VCM systems, the influence of the electrode material configuration is also pronounced, and is capable of modulating the active resistive switching interface. For both types of memory cells, the switching behavior changes significantly with variation of the oxide thickness. The results present important materials selection criteria for rationale design of ReRAM cells for various memristive applications.

1. Introduction

Driven by the growing demand for big data storage and emerging applications like the Internet of Things[1,2] and artificial intelligence,[3–5] high-density and energy-efficient memories are highly desired.[6,7] Conventional memory technologies, such as dynamic random access memory (DRAM) and flash memory are reaching the physical scaling limits. To tackle this problem, emerging memory technologies have been proposed during last years.[8–10] Among them, redox-based resistive random access memories (ReRAMs) have received special attention for its CMOS-compatible fabrication, performance, multi-functionality and scaling potential.[1,11,12] It is recognized important building block for next generation storage memories, computation-in-memory architecture and artificial intelligence.[3,8,10–12] ReRAM is a two-terminal metal–insulator–metal cell. The electrical conductivity of the insulating layer, typically a transition metal oxide, can be tuned by ionic modulation, caused by external electrical stimulation.[11] The oxide film has the ability to conduct ions such as metal cation, protonic charge and oxygen ions/vacancies, therefore it is often referred to as solid electrolyte.[13–15] Depending on the functional principles, two type ReRAMs are particularly promising—electrochemical metallization memory (ECM) and valence-change memory (VCM).[11,16,17] The resistive switching in ECM cells relies on a metallic filament that forms, and respectively dissolves, between the active electrode and counter electrode.[16] The formation of filament corresponds to a SET process, during which the cell switches from high resistive state (HRS) to low resistive state (LRS). The SET process is accompanied by multiple individual electrochemical processes, i.e., ionization (oxidation) of active electrode, diffusion of metal cation in the oxide electrolyte and nucleation/growth at counter electrode. The application of reverse potential switches the cell back to HRS by oxidizing/dissolving the filament, resulting in a RESET process. Electrochemically active metals, such as Ag, Cu, or their alloys/compounds are typically employed as active electrodes.[13,18,19] The counter electrode is made by inert materials like Pt, Ir or compounds such as TiN.[18–20] VCM cells consist of bottom electrode with high work function (e.g., Pt, TiN) which forms a Schottky interface with the oxide. The top electrode is electrochemically active, typically metal with high oxygen affinity (e.g., Ta, Ti, Hf) which allows redox reactions/ion exchange and forms an ohmic contact to the oxide, favoring the oxygen vacancy defect formation.[21,22] It is widely accepted that the resistive switching for VCM cell is achieved by modulating the electrostatic barrier at Schottky interface by migration and redistribution of oxygen vacancy defects.[11,23]

S. Chen, I. Valov
Institut für Werkstoffe der Elektrotechnik II
RWTH Aachen University
Sommerfeldstraße 24, 52074 Aachen, Germany
E-mail: i.valov@fz-juelich.de
I. Valov
Peter Grünberg Institut 7 and JARA-FIT
Forschungszentrum Jülich
Wilhelm-Johnen-Straße, 52425 Jülich, Germany
The ORCID identification number(s) for the author(s) of this article can be found under https://doi.org/10.1002/adma.202105022.

© 2021 The Authors. Advanced Materials published by Wiley-VCH GmbH. This is an open access article under the terms of the Creative Commons Attribution-NonCommercial-NoDerivs License, which permits use and distribution in any medium, provided the original work is properly cited, the use is non-commercial and no modifications or adaptations are made.

DOI: 10.1002/adma.202105022

Over the last decade, significant efforts have been made toward understanding the electrochemical processes in ReRAM devices and performance optimization. For instance, in ECM cells cyclic voltammetry have been employed to study the half-cell redox reactions and ion migration.[24–27] The metallic filament formation and dissolution were revealed by in situ and ex situ transmission electron microscope.[15,28–31] The impact of relative humidity level, active electrode material composition, catalytic activity of the counter electrode, as well as oxide materials on resistive switching behavior and device reliability have also been studied by above techniques.[18,24,27,32] In VCM cells, significant progress has also been made regarding the understanding of oxygen vacancy defect formation, migration[15,33] and cell switching stability.[34,35] Multiple approaches such as selecting ohmic electrode material with proper defect formation energy,[36,37] applying multilayer oxides,[21,38,39] have been attempted to improve cell performance. However, in most of the reported works, the conclusions were drawn based on studies containing only one type of variable, either the specie of active (ohmic) electrode material, or the counter (bottom) electrode material, overlooking the comprehensive analysis considering the configuration/combination of the electrode/electrolyte materials as a system. Besides, other important issues, for instance, the effect of active/ohmic electrode thickness in ECM/VCM cells, is rather scarce. Most important, to our knowledge, the impact of capping film material on electrochemical processes and switching behavior has not been considered.

In this study, we investigate the influence of electrode and capping layer materials configuration in HfO_2-based ECM and VCM cells of the type TiN(Pt)/Cu(Ti)/HfO_2/TiN(Pt). HfO_2 is selected as switching film due to its CMOS compatibility and wide use as an insulating layer for ReRAM devices. The thickness dependence of active and ohmic electrode materials and HfO_2-film are also studied. For both memory systems, different configurations with TiN and Pt as bottom electrodes and/or capping materials have been tested, keeping constant the active/ohmic electrodes. Cyclic voltammetry and current-voltage (*I–V*) sweeps are employed to study the electrochemical redox processes and resistive switching behavior, respectively. The results show the importance of selecting proper combination of oxide and active(ohmic) electrode thicknesses. Particularly, the modulation of resistive switching characteristics by varying capping layer material in a combination with counter(bottom) electrode configurations are demonstrated.

2. Results and Discussion

Figure 1 depicts the schematics of the different cell configurations and varied parameters we have used for this study for ECM and VCM types ReRAMs.

2.1. Electrochemical Metallization Memory

2.1.1. Identification of the Redox Reactions

Cyclic voltammetry measurements are performed by applying periodic triangular voltage sweeps to the cell. To obtain reliable cyclic voltammograms (CVs), proper potential ranges are

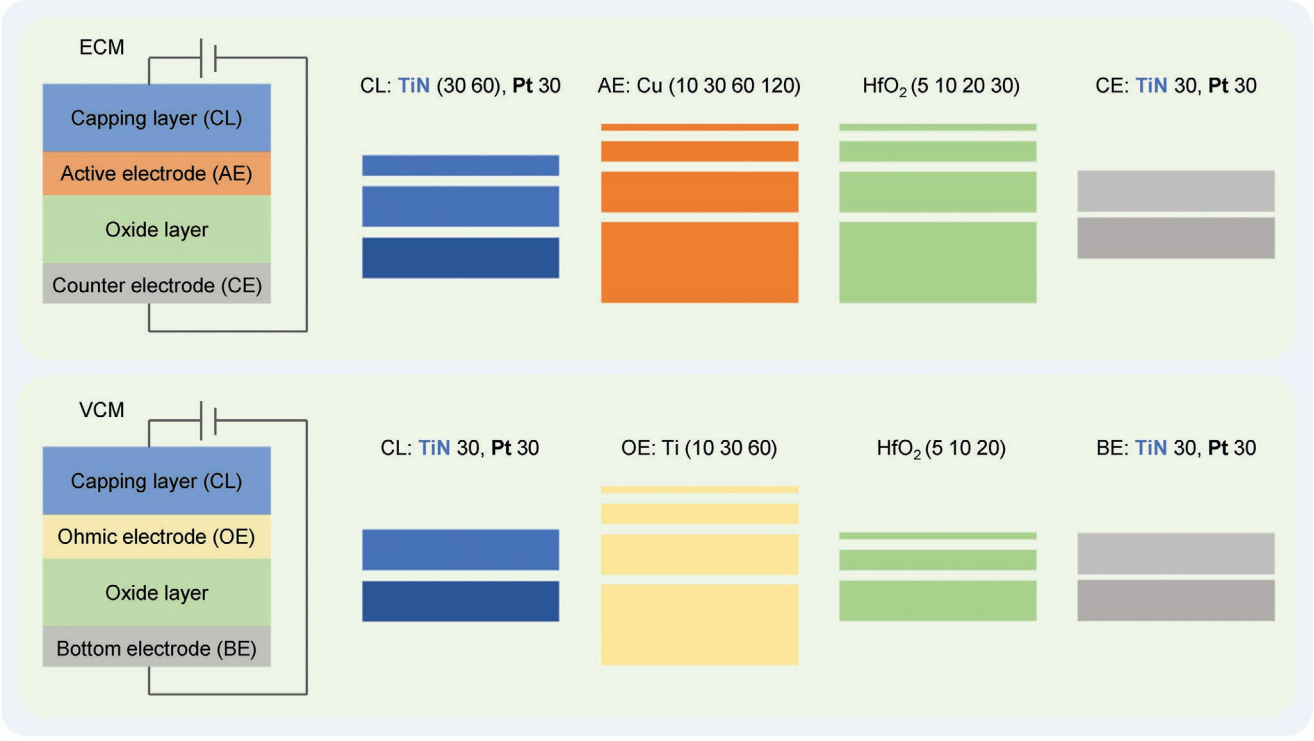


Figure 1. Schematic illustrations of ECM and VCM cell configurations. Detailed layer information and electrode materials are displayed on the right. The thickness (in nanometers) of each layer is also indicated.

© 2021 The Authors. Advanced Materials published by Wiley-VCH GmbH

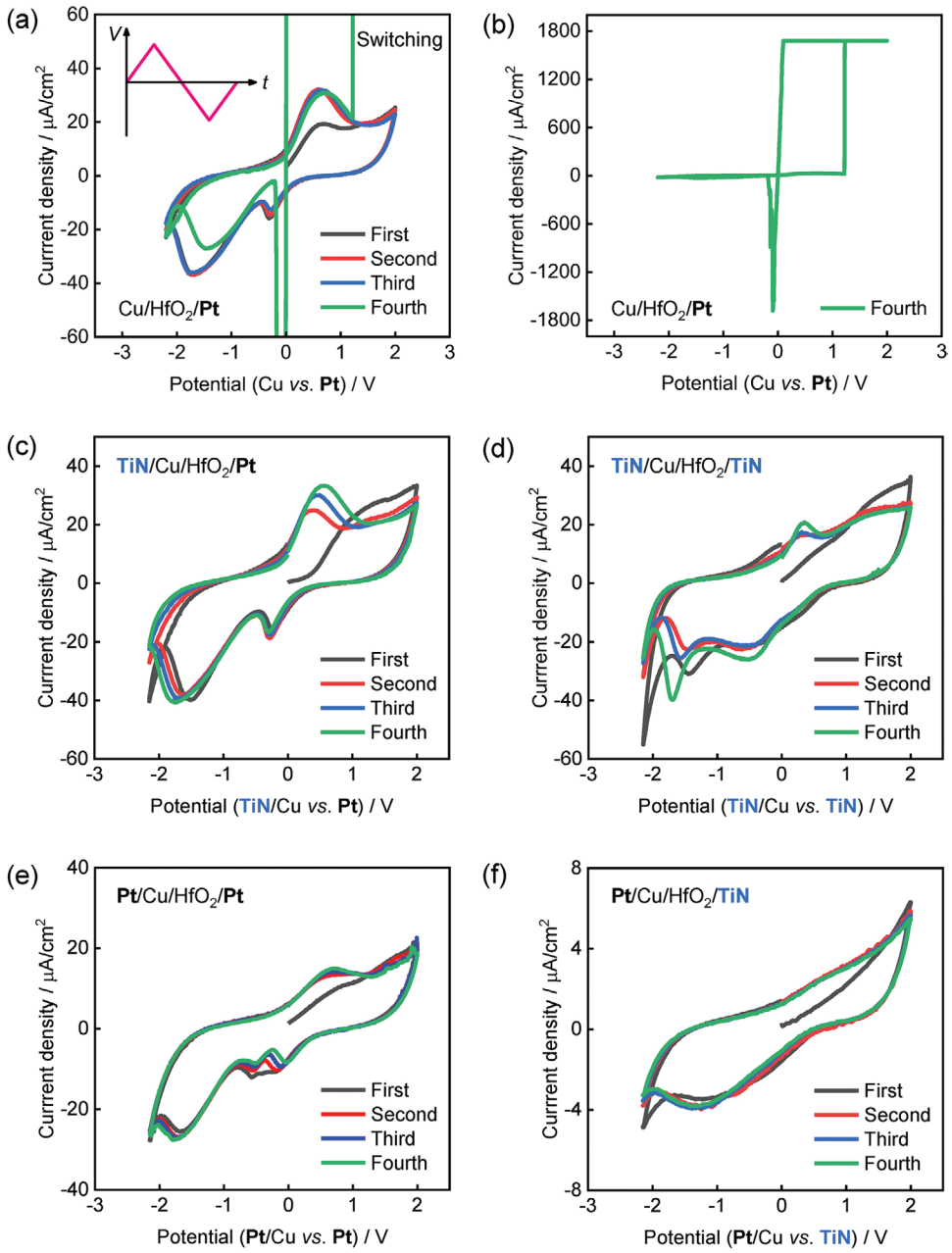


Figure 2. Cyclic voltammograms of ECM cells. a) Exemplary cyclic voltammograms for a $Cu/HfO_2/Pt$ cell. The inset shows the timing scheme of applied potential for CV sweeping. The cell undergoes resistive switching during the fourth sweep. b) Enlarged CV characteristic during the fourth sweep in (a), showing the cell switches from HRS to LRS during the positive voltage sweep, and switches back to HRS during the negative voltage sweep. c–f) Cyclic voltammograms of Cu/HfO_2 cells with varied electrode configurations. Four CV curves have been shown for each cell. For all CV measurement, the sweep rates are 74 mV s^{-1}.

selected to avoid the nucleation of metal ions and formation of metallic filament in the oxide electrolyte.[20,24] Additionally, current compliance is used to protect the cell from irreversible breakdown. Exemplary CV curves of $Cu/HfO_2/Pt$ cell are shown in **Figure 2**a. The pronounced current density peaks observed in the positive and negative sweeps are associated with the oxidation and reduction of the Cu electrode, respectively. As the positive potential increases, anodic oxidation of Cu to Cu ions starts at Cu/HfO_2 interface.

$$Cu \rightarrow Cu^{z+} + ze^{-} \quad (1)$$

Simultaneously under the electric field and concentration gradients, the generated Cu ions are injected into the oxide. Depending on the different valence states of copper ions, multiple oxidation and reduction processes (peaks) could be observed from the CVs. As the number of sweeps increases, increasing current density can be seen due to increased Cu ions incorporated into the HfO_2 electrolyte. The vertex potential is

© 2021 The Authors. Advanced Materials published by Wiley-VCH GmbH

limited to 2 V to prevent nucleation of Cu at HfO_2/Pt interface and further growth of Cu filament in the oxide layer. During the subsequent negative potential sweeps, the Cu ions are reduced back to Cu. However, not all incorporated Cu ions can be completely extracted during the negative cycles and thus accumulate, leading to lowering of the SET voltage. This phenomenon is observed in Figure 2a (the fourth CV sweep), where the cell exhibits an abrupt increase of current density at $V = 1.22$ V, indicating a SET process. A complete bipolar resistive switching cycle (SET + RESET), associated with the formation and disruption of Cu filament in the oxide electrolyte was observed (Figure 2b). This behavior is an illustration of the influence of several overlapping electrochemical effects on the resistive switching in ECM cell, directly correlated to active electrode redox reactions. It is a progressive electrochemical process accompanied by metal ionization at active electrode, cations diffusion (and in many cases accumulation) within the oxide electrolyte, and nucleation and growth at counter electrode interface.

CV characteristics obtained from Cu/HfO_2-based cells using different counter electrodes and capping layer configurations, are shown in Figure 2c–f. The thicknesses of the counter electrodes and capping layers are kept the same, i.e., 30 nm. For all cases, the first four CV curves are shown. Cells with different electrode configurations show different CV characteristics. However, from the number of peaks, their position and intensity, the metal species, and redox reactions that the active electrode undergoes can be deduced. For TiN/Cu/HfO_2/Pt cell (Figure 2c) the CV shows initially an oxidation peak at $V \approx 1.3$ V and distinctive reduction peaks at $V \approx -0.28$ V and $V \approx -1.62$ V. In the following sweeps pronounced second oxidation process is detected at $V \approx 0.36$ V, whereas the reduction peaks remain with nearly unchanged intensity. In aqueous solutions, the standard redox potentials for Cu electrode are given as Cu^+/Cu ($E^{\phi,1} = 0.52$ V), Cu^{2+}/Cu ($E^{\phi,2} = 0.34$ V), Cu^{2+}/Cu^+ ($E^{\phi,3} = 0.16$ V).[40] Although the Cu ions in this study are dissolved in solid electrolyte, the general trend of redox potentials is considered to remain unchanged.[26] We attributed the first oxidation peak (at $V \approx 0.36$ V) to Cu^+ to Cu^{2+} oxidation, which is the most thermodynamically favorable. The second peak represents Cu to Cu^{2+} reaction. The first reduction peak we associate to Cu^+ to Cu reaction. During the first CV sweeping, Cu to Cu^+ oxidation is taking place after the appearance of first current density peak. However, it is not directly detectable in the first sweep in positive voltage range. The current density peak would be observed beyond the applied vertex potential, but this is masked by the starting filament formation/switching. The second reduction peak could represent either Cu^{2+} to Cu, or Cu^{2+} to Cu^+ reduction. The third redox reaction also takes place but cannot be resolved as individual peak at this device configuration. We found that the sensitivity of the CVs can be improved by changing the Pt counter electrode by TiN. Two oxidation peaks (Cu^+ to Cu^{2+} and Cu to Cu^{2+}) at $V \approx 0.36$ V and $V \approx 1.3$ V and three reduction peaks at $V \approx 0.35$ V (Cu^+ to Cu), $V \approx -0.56$ V (Cu^{2+} to Cu), and $V \approx -1.48$ V (Cu^{2+} to Cu^+), respectively, could be clearer differentiated (Figure 2d), thus confirming indirectly the presence of third redox reaction of Cu to Cu^+ also in the positive potential sweep cycle.

2.1.2. Influence of Counter Electrode and Capping Layer Materials

Electrochemical Redox Reactions and Ion Transport: The influence of the counter and active electrode materials as individual components on the electrochemical and switching kinetics has been studied in several recent works, e.g., refs. [18,24,25,41,42]. Here, we observed, that the combination of counter electrode and capping layer materials (of the active electrode) play substantial role as well for the electrochemical processes and as well for the switching behavior. **Figure 3**a depicts CVs for different material combinations. For better classification, the second CV curve is selected for the comparison. For cells using TiN as counter electrode and Pt as capping layer (Pt/Cu/HfO_2/TiN), the current densities are much smaller than for the other types of cells (Figure 2f). The redox processes are suppressed and only one broad oxidation peak ($V \approx 0.65$ V) and one reduction peak ($V \approx -1.2$ V) were recorded. When the CE is exchanged to Pt (Pt/Cu/HfO_2/Pt), higher current densities were observed again, the redox processes become much faster, and three reduction peaks are observed (Figure 2e) in the subsequent CV sweeps. TiN-capped devices always show more intensive current density peaks and higher current density compared to samples using Pt as capping layer.

In previous publications, it has been demonstrated that the counter electrode half-cell reaction is essential in retaining overall electroneutrality in the system. Specifically, in ambient conditions it is realized by the reduction of moisture at HfO_2/CE interface

$$2H_2O + 2e^- \rightleftharpoons H_2(g) + 2OH^- \quad (2)$$

The ionization of Cu at active electrode interface (Equation (1)) needs to be coupled with the water-molecule reduction at counter electrode interface (Equation (2)) at least until Cu-ions reach the counter electrode. Therefore, the reaction rate is supposed to be influenced by the water partial pressure (pH_2O). To eliminate this factor our experiments were performed at constant humidity levels of ≈35%. Thus, all differences in device behavior and performance were directly attributed to the different electrocatalytic properties of the counter electrode and the permittivity of the capping layers. Pt is reported to have higher electrocatalytic activity than TiN toward water reduction.[41,42] To substantiate this, we calculated the ionic charge incorporated, respectively its concentration, into the device by integrating the current peak at positive potential sweep of first cyclic voltammogram[20] and dividing it by the cell geometry (see Experimental Section)

Figure 4a shows the calculated ion concentrations as a function of material configurations of the devices. Cells using Pt as counter electrode, and as well cells using TiN as capping layer, show relatively high ion concentrations. The lowest concentration is obtained for Pt/Cu/HfO_2/TiN devices, which is in agreement with the observations in cyclic voltammograms (Figures 2f and 3a) and forming voltages (Figure 3b), in which these cells show lowest current densities and highest forming voltages. The diffusion coefficient (D_{ox}) of Cu ions is also calculated using the Randles–Sevcik equation[43]

$$j_{p,red} = 2.99 \times 10^5 \cdot z^{3/2} c_{ion} \cdot \sqrt{\alpha D_{ox} v} \quad (3)$$

© 2021 The Authors. Advanced Materials published by Wiley-VCH GmbH

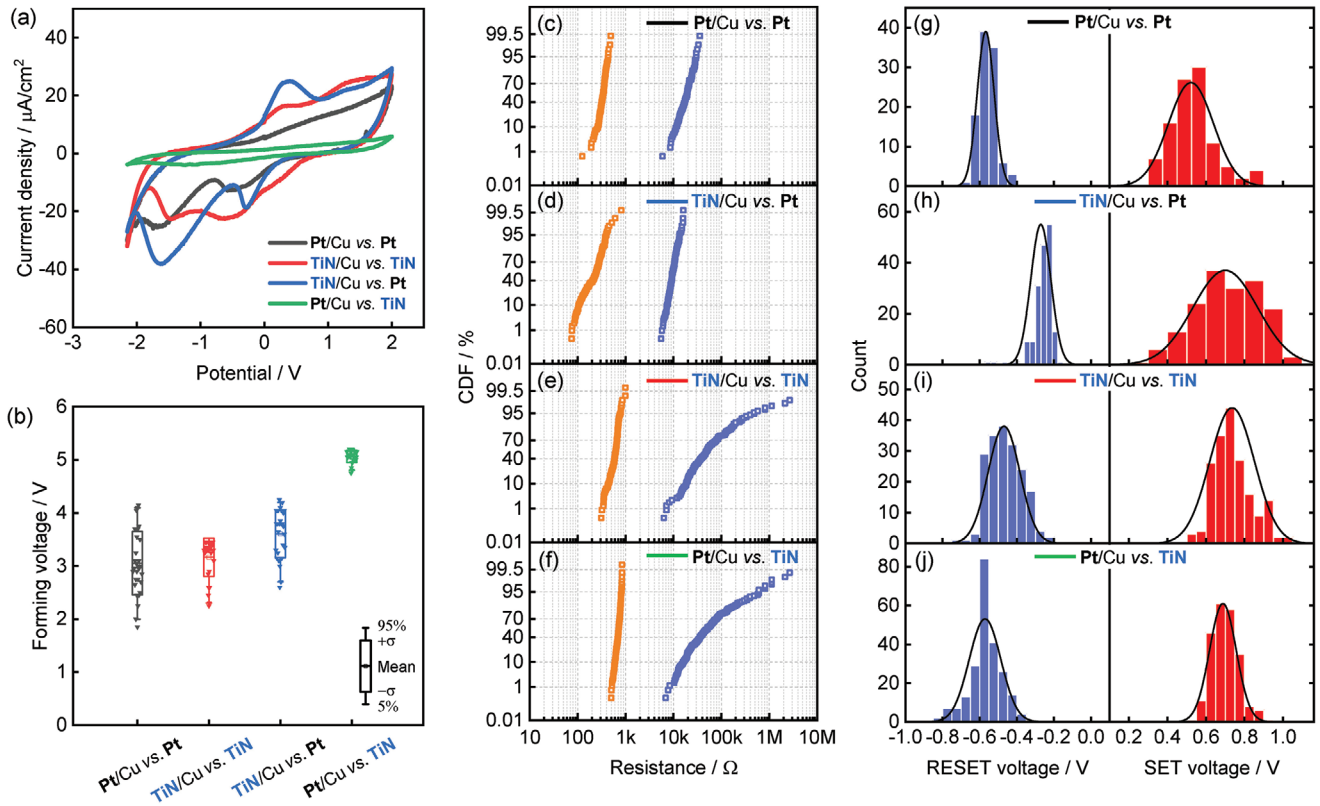


Figure 3. Comparison of cyclic voltammograms and resistive switching characteristics. a) Comparison of cyclic voltammograms of Cu/HfO_2 cells with varied electrode configurations. For all the cells, the second CV curve is shown. b) Comparison of forming voltages. Each box contains forming voltages from thirty distinct cells. The inset figure shows the definition of the box chart. c–j) Comparison of LRS, HRS resistance (c–f) and SET, RESET voltages (g–j). The evaluation is conducted on the *IV* curves collected from five distinct cells (35–40 *IV* curves each) for each type of configuration. For Pt/Cu/HfO_2/Pt cell configuration 20 *IV* curves each. Exemplary *IV* curves are shown in Figure S1, Supporting Information.

where $j_{p,red}$ is absolute current density of the first reduction peak, $z = 2$ the number of electrons transferred in the redox reaction (assume the Cu^{2+} is the dominating ion specie in the oxide), c_{ion} the concentration of copper ions, $\alpha \approx 0.5$ the charge transfer coefficient,[44] $\nu = 74$ mV s^{-1} the sweep rate. As shown in Figure 4b, the diffusion coefficient for cells with Pt counter electrode are higher than that of TiN. The Pt/Cu/HfO_2/Pt cell shows highest diffusion coefficient. By comparing the cells that contain identical counter electrode, higher ion concentration leads to a decrease in diffusion coefficient. This is particularly pronounced for cells with TiN counter electrode, where the Pt/Cu/HfO_2/TiN cell shows lowest ion concentration yet depicts higher diffusion coefficient than TiN/Cu/HfO_2/TiN. Therefore, for cells containing high concentration of Cu ions, the ion–ion

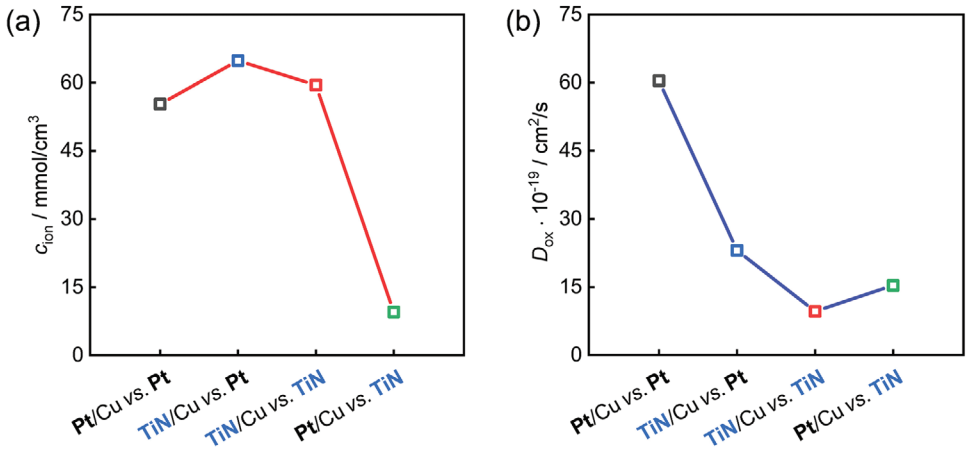


Figure 4. a,b) Calculated ion concentration (c_{ion}) (a) and diffusion coefficient (D_{OX}) (b) in Cu/HfO_2 cells with varied counter electrode and capping layer.

© 2021 The Authors. Advanced Materials published by Wiley-VCH GmbH

interactions, which has been reported in Cu/SiO_2 and Cu/Ta_2O_5 ECM cells, has to be considered.[24,45] In particular, the ion concentrations in Cu/HfO_2 cells are more than one order of magnitude higher than the values reported in SiO_2 and Ta_2O_5. The ion–ion interactions lead to the decrease of ion mobility and in turn inhibit the Cu ionization at active electrode interface.

Switching Processes: To understand the impact of redox processes on the resistive switching behavior, *I–V* sweeps are subsequently performed inducing SET/RESET events in the cells. Similar to CV sweeping, triangular voltage pulse is applied, whereby the vertex potential is set to be high enough to trigger the forming process. In general, faster redox reaction rate will accelerate the formation of metallic filament, as more metal cation ions are generated and diffused into the oxide electrolyte. The forming voltages of the different cell configurations are summarized in Figure 3b. For cells showing distinctive redox peaks (TiN capped cells and $Pt/Cu/HfO_2/Pt$, Figure 3a), the forming voltages show no remarkable difference. While the $Pt/Cu/HfO_2/TiN$ cells show highest forming voltages.

The statistic evaluation of the resistance values at HRS and LRS (read at $V = 0.1$ V), as well as SET and RESET voltages are shown in Figure 3c–j. When Pt is utilized as counter electrode, the HRS resistance is particularly stable, the cumulative distribution function (CDF) shows to be very uniform with less than 1 order of magnitude fluctuation (Figure 3c,d). The influence of capping layer is also noticeable. The overall resistance for TiN capped cells is lower than Pt capped cell (CDF curves shift to the left by comparing Figure 3d with Figure 3c). The SET voltages are found higher, yet the RESET voltages are lower in contrast to Pt capped cells (Figure 3g,h). The direct comparison SET/RESET voltages can be found in Figure S1b, Supporting Information.

When TiN counter electrode is used, the HRS resistance is very unstable and shows 2–3 orders of magnitude variation during cycling. Another trend that can be identified is that, as CE is changed to TiN, both the LRS and HRS resistance are increased, as depicted by the CDF plot (CDF curves shift to the right, see Figure 3e,f). This indicates the overall resistance in TiN CE-based cells is higher than that of Pt, regardless the difference in capping electrode material.

The observations clearly demonstrate that both counter electrode and capping electrode materials influence the resistive switching characteristics. The counter electrode determines the total resistance, where both LRS and HRS resistance are lower for devices using Pt counter electrode. The capping electrode is additionally modulating the resistance states.

The value of the LRS resistance reflects the size of formed metallic filament. Larger size of filament will result in lower LRS resistance.[11] The HRS reflects indirectly the stability of the formed filament. If the filament is fully dissolved by the RESET voltage and most cations are reduced/extracted, higher HRS resistance will be obtained. As a result, the SET voltage in the subsequent *I–V* sweep will be increased. This scenario requires higher driving force (voltage) and/or longer time. On the contrary, if the filament is only partially dissolved, or cations are accumulated in the switching layer, the HRS resistance after RESET will be lowered. The electrical field in the residual filament region is still high, and directly a filament growth will start on the basis of the residual Cu whisker, instead of nucleation at the counter electrode interface, followed by growth.

The Role of the Counter and Capping Electrodes: The electrocatalytic activity of counter electrode is the limiting factor for overall cell resistance. It can directly influence the counter electrode half-cell reaction, which corresponds to water molecule reduction at oxide/counter electrode interface. As Pt has higher electrocatalytic activity than TiN,[41,42] it facilitates not only the water molecule reduction and persistent Cu ionization at active electrode interface, but also ensures faster Cu ion-reduction/nucleation. Higher ion concentration and faster diffusion coefficient are achieved (in contrast to cells with TiN CE), accelerating the nucleation and growth at counter electrode. Larger size of metallic filament is more likely to be formed, resulting in decrease of overall cell resistance (Figure 3c,d). Furthermore, due to the large filament size and low LRS resistance, the RESET process can result in partially dissolution of the filament, making the HRS resistance rather stable. The application of TiN as capping layer can further decrease the overall cell resistance (Figure 3d,e), as more metal ions are produced upon oxidation at active electrode interface (Figure 4a). In this case the RESET voltages are reduced by increased Joule heating (see Figure 3h,i),[22] although the complete RESET is still difficult and the SET voltages are increased as the diffusion coefficient of Cu ions is reduced (Figure 4b). We related the increased conductivity (higher Cu ion concentration) observed in TiN capped cells to the clean interface: capping electrode/Cu by using TiN. A general problem in the Cu-based metallic bilayer systems is the interdiffusion at the interface. For example, in Pt/Cu bilayer structure, the diffusion of Pt into Cu and/or Cu outdiffusion into Pt can lead to the formation of new solid phases at the Pt/Cu interface, degrading the cell conductivity and inhibiting Cu ion diffusion into the HfO_2 film.[46,47] Whereas the interdiffusion between TiN/Cu is negligible due to the limited solubility of Cu into TiN.[46] The interdiffusion phenomenon of Pd–Cu, Pt–Cu, and other Cu-based bilayer films have been well documented in the literature.[46–48] Thus, the interdiffusion effect should be carefully considered when utilizing different metals as capping electrode for Cu. The same effect is expected to be present for other material systems and therefore possible interactions between active electrodes and capping layers should be always taken into account by materials selection.

2.1.3. Influence of the Thickness of Active Electrode and Capping Layer

The resistive switching in ECM cells depends on active electrode ionization, cation accumulation and migration in the oxide, and reduction, nucleation and growth at counter electrode interface. The active electrode serves as metal cation reservoir and may determine the cation concentration in the whole device. We studied the dependence of cell performance on the thickness of the Cu layer in Cu/HfO_2 (10 nm)/Pt devices. **Figure 5**a depicts cyclic voltammograms of structures with multiple Cu electrode thickness. The CV curves show small variation in redox peak potentials, implying all cells undergo identical electrochemical processes. The current densities in the CV (Figure 5a) increase with Cu thickness increasing from 10 to 60 nm, indicating

© 2021 The Authors. Advanced Materials published by Wiley-VCH GmbH

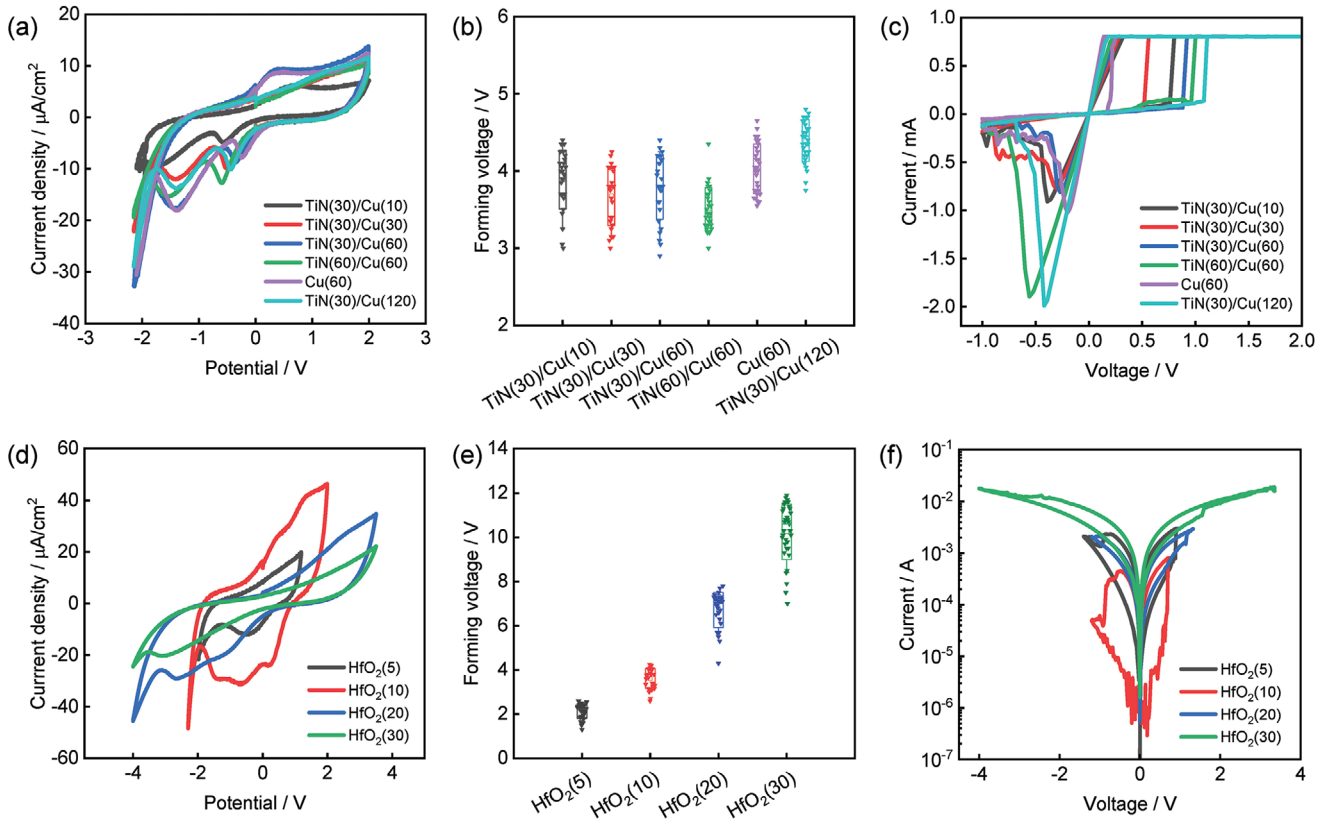


Figure 5. Impact of active electrode thickness and oxide thickness in ECM cells. a) Cyclic voltammograms of TiN/Cu/HfO_2 (10 nm)/Pt devices with varied Cu thickness. To more clearly distinguish the redox processes, the sweep rates are kept at 30 mV s^{-1} for all cells. b) Comparison of forming voltages. c) Exemplary *I–V* curves measured from devices of (a). d) Cyclic voltammograms of HfO_2 ECM devices with different HfO_2 thickness. To hinder the forming for a 5 nm HfO_2 cell, the sweep rates are increased to 125 mV s^{-1}. e) Comparison of forming voltages. f) Exemplary *IV* curves measured from the devices in (d).

more Cu cations are generated. However, the current density decreases for 120 nm Cu.

The statistic evaluation of forming voltages suggest no pronounced difference with varied Cu thickness, despite the cells with 120 nm Cu shows slightly higher forming voltages.

Figure 5c depicts exemplary *I–V* switching showing no pronounced change in resistive switching behavior. However, the cycling uniformity is affected, as shown in Figure S2, Supporting Information. Devices with 30 nm Cu provide the most reliable resistive switching. For the cells with 10 nm Cu, the variability in SET voltage is rather high. From the CV measurement it can be concluded that for these cells Cu electrode is not able to supply sufficient number of metal cations and form stable filament. Moreover, beside chemical dissolution, the physical (mechanical) stability of the active electrode must be considered. It has been reported that due to enhanced surface energy contribution nm-thin metal films can disconnect to metal clusters and even move into the electrolyte, degrading mechanical and electrical contact, resulting in instability of threshold voltages during resistive switching.[49] On the other hand side too thick metal electrode, in our case 60 nm and above can result in excessive generation of metal cations and form thicker metallic filament and a reliable RESET is rather difficult. It should be mentioned that the cells without TiN capping—in this case where the top electrode is 60 nm Cu—show relative low variation in SET and RESET voltages (Figure 5c; Figure S2, Supporting Information), but the cycling endurance is rather poor due to RESET failure. It can be also attributed to the excessive creation of Cu-ions leading to irreversible breakdown. In addition, due to the absence of capping layer, the Cu is more likely be get passivated when exposed in ambient condition. In particular, the passivation process can be accelerated when the voltage potentials are applied directly to the metal. TiN is favored as protective electrode due to its ability to block oxygen, although the possible TiO_x and TiON should also be considered. We notice the redox processes do not vary with the employ of TiN (see Figure 5a) thus the capping layer is less likely to get passivated during the time of our experiments.

The thickness of the capping layer (30 and 60 nm were tested) appears also to play a role in electrochemical and forming processes. However, this dependence requires further detailed study.

2.1.4. Influence of the Oxide Layer Thickness

The thickness of HfO_2 switching layer is found playing decisive role in cyclic voltammograms and resistive switching (Figure 5d–f). All devices are showing the redox peaks in the CVs, however, their intensities change and as well the

© 2021 The Authors. Advanced Materials published by Wiley-VCH GmbH

possibility to distinguish them (see also Figure S3, Supporting Information). For low oxide thickness (5 nm HfO_2) the electric field is the highest but also the electronic leakage currents are high. The peaks in the CV are clearly presented but the voltage range must be reduced in order to avoid switching. Thicker layers (20 and 30 nm) increase the total resistance and the redox peaks in Figure 5d are less pronounced. The electronic leakage currents are lower, but higher voltage (energy) is required to achieve same field strength and produce Cu-ions. An optimum performance is observed for the 10 nm HfO_2 device. It is thick enough to suppress high leakage currents but is sufficiently thin to allow easier oxidation of Cu electrode, incorporation and field-accelerated migration of active ions.

The switching behavior is following the same trend. Despite bipolar resistive switching is observed for all cases, the corresponding *I–V* characteristics differ remarkably. The forming voltages increase with increasing HfO_2 thickness in order to achieve the required electric field.

SET and RESET processes and the entire switching behavior is found sensitive to a combination of three factors—leakage currents, field strength and the forming procedure. The 5 nm HfO_2 cells show small forming voltages at $V \approx 2$ V. However, because of the high electronic leakage currents (low ionic transference number) it requires higher voltages for SET operation (compared to 10 nm HfO_2 device). Besides, the cells undergo RESET failure easily due to the generation of excessive metal ions driven by the high electric field in the oxide film. For cells with oxide thickness of 20 and 30 nm, owing to the high forming voltages, obtaining reliable resistive switching is challenging. The cells are damaged easily during the aggressive forming process. The 10 nm devices present a compromise between these factors and are characterized by most reliable operation and highest OFF/ON resistance ratio.

2.2. Valence-Change Memory

For VCM devices the measurements are carried out on Ti/HfO_2-based cell configurations. As bottom electrodes, high-work-function materials—Pt and TiN—are employed. The ohmic electrode was Ti metal that has high oxygen affinity and scavenges oxygen from HfO_2 to support the filament formation. Ti electrode was protected from oxidation when exposed to ambient atmosphere by TiN or Pt capping layers. **Figure 6**a–h shows cyclic voltammograms and *I–V* characteristics of devices with different electrodes/capping layer configurations.

2.2.1. Electrode Redox Reactions in VCM Cells

In valence-change memories (as in the case of ECM) redox reactions are playing essential role. In our devices of the type

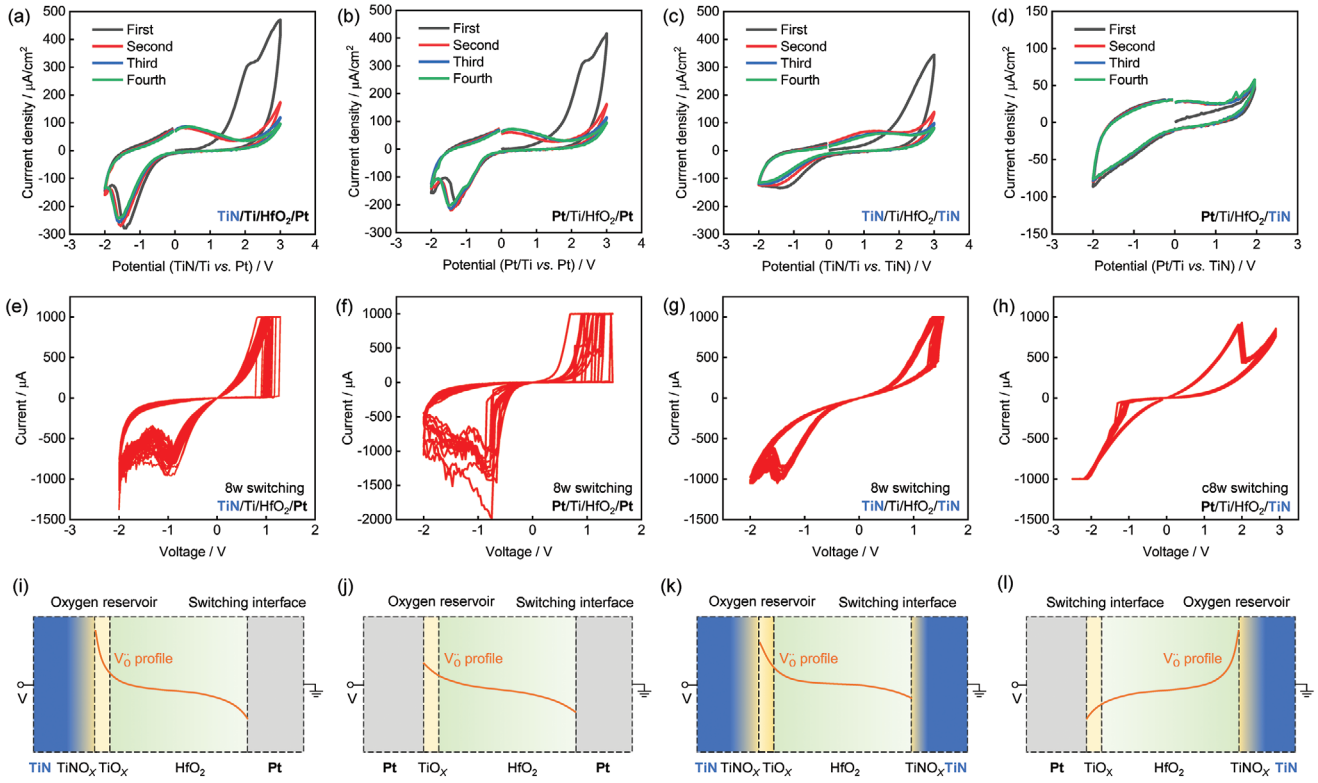


Figure 6. Impact of electrode material on VCM switching. a–d) Cyclic voltammograms of cells with different configurations. In all cases, the Ti thickness and HfO_2 thickness are 10 nm, the thickness of the capping electrode and the bottom electrode are 30 nm. The sweep rates are 710 mV s^{-1}. The voltage sweeping range was selected in a way to avoid forming of the devices. e–h) The corresponding *I–V* curves of each cell configuration. i–l) Suggested distribution of oxygen vacancy profile along the oxide at HRS (after forming). It indicates the impact of the capping and bottom electrode materials on oxygen-vacancy formation and distribution profile in the oxide layer. The density of oxygen vacancies at the oxygen reservoir layer is higher than that of the active switching interface.

© 2021 The Authors. Advanced Materials published by Wiley-VCH GmbH

TiN(Pt)/Ti/HfO_2/Pt or TiN(Pt)/Ti/HfO_2/TiN the FORM process includes two half-cell reactions. At the active/ohmic electrode the reaction is

$$Ti \rightarrow Ti^{x+} + xe^- \quad (4)$$

The number of exchanged electrons (x), respectively the resulting oxidation state of the metal cations depend on the applied voltage and the local environmental conditions, e.g., temperature, water partial pressure, oxygen partial pressure, etc. The amount of oxidized metal atoms (depend on the electrode surface area and thickness) and its valence state determine the oxygen scavenging ability of the ohmic electrode, i.e., to accept oxygen ions (O^{2-}) overcoming the HfO_2/electrode interfacial barrier. The general equation is defined as

$$Ti - xe^- + \frac{x}{2}O^{2-} \rightarrow TiO_{\frac{x}{2}} \quad (5)$$

The ability of Ti to accept oxygen ions from the oxide electrolyte ends by reaching the compositin TiO_2 (complete oxidation).

The counter electrode reaction taking place at the Pt(TiN)/HfO_y interfaces can be: i) reduction of HfO_y, ii) reduction of oxygen, or iii) reduction of H_2O molecules. Details on the electrochemical processes associated to the counter electrode reactions at the Pt/HfO_y interface are provided in ref. [50].

After forming, the resistive switching in filamentary type VCM devices occurs in a small disc of thickness of approximately 2–3 nm by displacement of oxygen ions/vacancies and electrons between the filament tip and the Schottky electrode. This process is electrochemical in nature and involves change of the oxidation state of the Hf-ions within this disc. For the case that oxygen vacancies are depleted at the Pt/HfO_y interface (enriched with oxygen ions) at positive voltage applied to the Pt electrode the redox reaction is given by the equation

$$HfO_y - xe^- + \frac{x}{2}O^{2-} \rightarrow HfO_{\frac{2y+x}{2}} \quad (6)$$

where y is the initial oxygen stoichiometry of the oxide film and x is the number of exchanged electrons. The condition $2y + x = 4$ must be fulfilled.

Due to the oxidation reaction, the Schottky barrier at this interface is increased.

In the same time at the other interface: HfO_y/HfO_z (HfO_z represents the filament tip with $z < y$) HfO_y will be reduced according to

$$HfO_y + xe^- - \frac{x}{2}O^{2-} \rightarrow HfO_{\frac{2y-x}{2}} \quad (7)$$

Reactions 6 and 7 are coupled and lead to RESET process. For SET event the bias needs to be reversed, thus reversing the direction of reactions 6 and 7, restoring the stoichiometry HfO_y within the switching volume.

Exact identification of the kinetic parameters of reactions 4–7 in our systems (e.g., number of exchanged electrons, oxidation state of the cations and oxygen stoichiometry) is extremely challenging, as there are several possible intermediate states and only few of them with determined standard electrode potentials. Therefore, exact identification of the redox peaks was not possible. The peak positions on the voltage axes (related to the reversibility of the processes) and current densities (reaction rate) vary depending on the bottom electrode and capping electrode materials. This indicates the importance of material selection and materials combination for the electrochemical processes and related switching properties.

2.2.2. Influence of the Bottom Electrode and Capping Layer Materials

As it can be seen in Figure 6a, in the VCM cell using a Pt bottom electrode and a TiN capping layer (TiN/Ti/HfO_2/Pt), an oxidation current density peak is well resolved at $V \approx 2.1$ V in the first positive CV sweep. A strong reduction is coupled within the negative current density branch. The subsequent CV sweeps show reproducible oxidation peaks at $V \approx 0.35$ V with slightly higher reduction potentials at $V \approx -1.6$ V. Note that the current densities significantly decrease after the first CV sweeping. This is in line with previous findings, indicating Ti electrode undergoes passivation effect during the first cycle.[25,51,52] Afterward, the current densities decrease gradually with increasing number of sweeps, suggesting the ongoing oxidation of the Ti electrode. When Pt is used as the capping material (Pt/Ti/HfO_2/Pt), similar CV characteristics are observed (see Figure 6b). In comparison to Cu, the Ti metal has a higher affinity to oxygen, thus making it easier to undergo oxygen exchange reaction and form intermediate sub-stoichiometric oxide layer at the interface. This interfacial oxide is plausible to increase overall resistance of the cell and inhibit ion and electron exchange across the electrode/oxide interface, lowering the current density in cyclic voltammograms. The chemical formation of the interfacial oxide layer depends on two factors: exchange with underlying HfO_2

$$Me + O_o^{\times} \rightleftharpoons MeO_x + V_o^{\cdot\cdot} + 2e^- \quad (8)$$

but also the uptake of moisture from environment

$$Me + xH_2O \rightleftharpoons MeO_x + 2xH^+ + 2xe^- \quad (9)$$

Recent studies have shown moisture plays essential role in VCM cells by participating half-cell redox reactions.[50] For instance, the presence of moisture leads to an increase of cell conductivity (providing charges by Equations (2),(9)) and thus, accelerating ion migration and redox reaction rate.[45] A reliable forming process was found not possible in the absence of moisture.[50] The forming and SET voltages can be reduced with increasing humidity.[27] As mentioned earlier the humidity in this study is constant around ≈35%. Hence, herein we focus on electrode redox processes with the oxygen that decomposed from the oxide. The electrochemical incorporation/evolution of oxygen from HfO_2 into Ti metal with formation of reduced oxides can be also expressed in terms of point defects changes, coupling Equations (4)–(7) with

© 2021 The Authors. Advanced Materials published by Wiley-VCH GmbH

$$O_o^{\times} \rightleftharpoons V_o^{\cdot\cdot} + 2e^- + \frac{1}{2}O_2(g) \quad (10)$$

where oxygen vacancies are defined using Kröger–Vink notation.[53] It is important to notice that for SET and RESET processes, the increase of the number of oxygen vacancies must be compensated solely by electronic defects in order to reach the ON state.

By comparing the cyclic voltammograms (Figure 6a,b), we noticed that the current densities of Pt capped cells are lower than that of TiN. Since the only difference between the two cell configurations is the capping layer, we suggest that the decrease of current density is attributed to the interdiffusion effect of the capping layer. The corresponding *I–V* switching characteristics confirm the assumption. As can be seen in Figure 6e, the *I–V* curves of TiN capped cell exhibit higher cycle-to-cycle consistency, whereas Pt capped (Pt/Ti/HfO_2/Pt) cells show poor cycling endurance due to the high variation in SET voltages and high variability at LRS (Figure 6f). We suppose the differences are due to different O_2 and/or H_2O permeability of Pt and TiN and correspondingly the amount of oxygen vacancies generated in the oxide. Proper amount of oxygen vacancies defects is demanded to facilitate reproducible resistive switching. The higher current density and more reliable RS observed in Figure 6a,e indicates higher density of oxygen vacancies exists in the TiN-capped cells. From the applied voltage polarity and positions of redox peaks, it is possible to determine that the oxygen exchange processes take place at Ti/HfO_2 interface. In other words, the oxygen vacancies are prone to be accumulated at Ti/HfO_2 interface and move toward HfO_2/Pt interface during Forming and SET operations. Since both types of configurations consists of 10 nm Ti, we assume TiN is also involved in the redox reactions and leads to increase of oxygen reservoir capability. Although TiN is ideally supposed to be oxygen-inert, it has been reported that the oxygen scavenging capability of TiN can be remarkably enhanced due to formation of $TiNO_X$.[54] Pt is widely accepted that cannot be used as a scavenge layer when utilized as ReRAM electrode material.[11] To substantiate the assumption, Pt bottom electrode has been substituted by TiN, and TiN/Ti/HfO_2/TiN stacked cells are fabricated and characterized. The current densities (Figure 6c) decrease and redox peaks become broader, indicating slower redox reaction rate. By comparing the RS characteristics (Figure 6g) with TiN/Ti/HfO_2/Pt cells (Figure 6e), the SET and RESET voltages of the cells are increased, and the I_{LRS}/I_{HRF} is significantly reduced (see Figure S4a, Supporting Information). Based on above observations, it can be concluded that in contrast to Pt, TiN electrode is capable to influence redox processes/defect formation in VCM system. The fact that TiN/Ti/HfO_2/TiN cells show higher threshold (SET + RESET) voltages and smaller RS ratio could be attributed to the TiN bottom electrode undergoing oxygen ions exchange as well by scavenge oxygen and form an oxygen-rich $TiNO_X$ layer. This process can compete with the oxygen ions exchange at ohmic interface, thus decelerating the defect formation rate. Therefore, the oxidation current densities peaks shift to potential $V \approx 1.2$ V (Figure 6c) to counteract defect generation at HfO_2/TiN interface. This oxidation potential is much higher than those observed in Figure 6a,b. Ultimately, the total amount of oxygen vacancy defects created after forming is increased, which is proved by the observation of high RESET current (Figure S5c, Supporting Information). And more importantly, the Schottky barrier height at HfO_2/TiN interface and the oxygen vacancy concentration gradient in the oxide layer are lowered, causing a decrease of resistive switching ratio (Figure S4a, Supporting Information).

It is important to mention that we found the titanium layer get fully oxidized when exposed to ambient atmosphere in the absence of capping layer, and the forming was not possible in these cells.

2.2.3. Materials Determined 8w and c8w Switching

It should be noted that for the cells using Pt as a counter electrode, as well as TiN/Ti/HfO_2/TiN cells, eightwise (8w) bipolar resistive switching is obtained when the voltage potentials are applied to the top electrode (capping layer + ohmic electrode), while the bottom electrode is grounded (Figure 6e–g). Specifically, the SET process is induced when applying positive potential to top electrode, RESET process takes place within negative voltage sweeping (Figure S4a, Supporting Information). This observation is in line with previous studies, indicating the resistive switching takes place at Schottky interface (HfO_2/Pt and HfO_2/TiN) where the electrostatic barrier is modulated through drift and diffusion of oxygen vacancies (and related electronic defects).[22] Thus, for TiN/Ti/HfO_2/TiN stacked cells, the presence of both TiN and Ti makes the overall oxygen reservoir capability at Ti/HfO_2 interface stronger than that at HfO_2/TiN interface. The active switching interface does not change by substituting TiN bottom electrode by Pt.

Interestingly, by substituting TiN capping electrode by Pt, which leads to Pt/Ti/HfO_2/TiN stacked cells, counter-eightwise (c8w) resistive switching is obtained (Figure 6h), whereby the cell can be SET to LRS by applying a negative voltage, while a positive voltage resets the device to HRS (Figure S4b, Supporting Information). In this case, the forming is achieved by application of positive potential, where a soft breakdown of the oxide is realized (Figure S5d, Supporting Information) and the cell remains at HRS. This is in contrast to many other types of VCM cells, where the forming processes always induce hard breakdown (LRS) and high RESET currents, at negative voltage sweeping branch are needed to successfully reset the cells (Figure S5a–c, Supporting Information). This result implies transition of the active switching interface from oxide/BE interface to the ohmic interface for Pt/Ti/HfO_2/TiN stacked cells. In other words, the oxygen reservoir layer has been reversed from Ti/HfO_2 interface to HfO_2/TiN interface. The cyclic voltammograms of Pt/Ti/HfO_2/TiN cells reveal less active oxidation of Ti, no distinctive current density peaks are observed within positive current density branch (see Figure 6d and Figure S6a (Supporting Information)). The change of active switching interface is further confirmed by the reproducible RS when reversing the applied voltage polarity (Figures S6b and S7a,b, Supporting Information). Since Ti is not anodizing in this case, no passivation (no significant decrease of current after first CV) is observed (Figure S6b, Supporting Information). The current density increases with increased cycles, the oxidation current density peaks appear at $V \approx 1.2$ V (Figure S6b, Supporting

© 2021 The Authors. Advanced Materials published by Wiley-VCH GmbH

Information), indicating strong oxidation occurs at HfO_2/TiN interface. It proves that TiN electrode has higher oxygen reservoir capability than that of Pt/Ti. It is worth stressing that for the cells with other configurations, no c8w switching is observed, as the reversed forming always induce irreversible breakdown to the oxide (Figure S7c–e, Supporting Information).

Based on the obtained result and analysis, the oxygen reservoir capability, active switching interface, and schematic distribution of the oxygen vacancy profile along the cells are illustrated in Figure 6i–l. Since the TiN is found involved in the oxygen exchange process, we assume the 10 nm Ti has been completely oxidized to nearly TiO_2 after forming process. Moreover, from the result of Pt/Ti/HfO_2/Pt cells, it is known that the 10 nm Ti is not able to induce sufficient amount of oxygen vacancy defects for reliable resistive switching (Equations (4), (8)).

2.2.4. Effect of Ti Electrode Thickness

Figure 7a depicts the cyclic voltammograms of TiN/Ti/HfO_2/TiN cells with varied Ti thickness. TiN is utilized as capping and bottom electrode. Only the first CV is shown for comparison. More CV curves are provided in Figure S8 (Supporting Information). It is seen from Figure 7a that for 10 nm HfO_2-based cells, current density significantly increases by increasing the Ti thickness from 10 to 30 nm. The higher current density corresponds to faster redox reaction rate of Ti electrode and thereupon production of higher concentration of oxidized ions (still without reaching a point of complete oxidation). And more crucially, larger amount of oxygen vacancy defects is generated simultaneously in the oxide (shift the equilibria of Equations (4),(8) to the right). This is further evidenced by the lower forming voltage for the Ti (30) cell (Figure S9a, Supporting Information). For all cases, the current densities decrease gradually with increasing CV sweep, suggesting the successive occurrence of Ti oxidation. Further potential sweeping will result in forming process due to the massive generation of oxygen vacancies. By increasing the Ti thickness to 60 nm, similar cyclic voltammograms can be seen, although the current densities slightly decrease. From Figure 7b, it can be seen that for 10 nm HfO_2, Ti layers with 30 and 60 nm thickness are capable of forming an adequate amount of oxygen vacancies, and thus induce reproducible RS with sufficiently

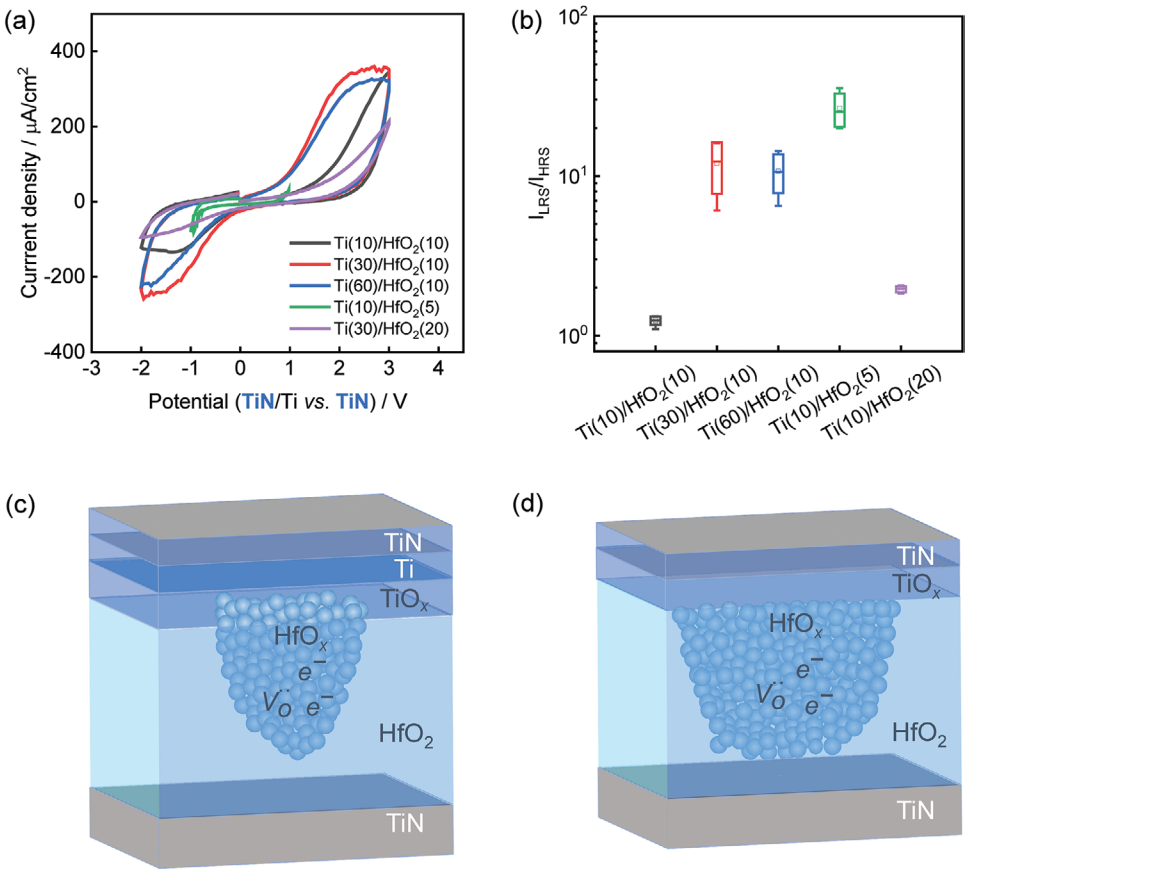


Figure 7. Impact of ohmic electrode thickness on VCM switching. a) The first cyclic voltammograms of cells with different Ti/HfO_2 stack thickness. More CV curves refer to Figure S8, Supporting Information. The sweep rates are 710 mV s^{-1}. b) Comparison of resistive switching ratio (I_{LRS}/I_{HRS}). c,d) Schematic illustration of oxygen vacancies distribution in Ti/HfO_2 cell. The Ti scavenges oxygen released from HfO_2, leaving behind oxygen-deficient HfO_x and generating oxygen vacancy defects. For the thin ohmic electrode in (d), Ti is prone to be completely oxidized during cell operation, and the overall resistance of the cell is increased, leading to higher forming potentials. As a result, excessive generation of oxygen vacancy defects can occur and making it difficult to reset the cell.

© 2021 The Authors. Advanced Materials published by Wiley-VCH GmbH

high OFF/ON ratio. In contrast, 10 nm Ti is too thin to induce enough oxygen vacancy defects in 10 and 20 nm HfO_2 layers. As a result, the resistance ratio is relatively small. For the 10 nm Ti/5 nm HfO_2 cell, the resistive switching ratio is improved. Note that in Figure 7a, the current density for 5 nm HfO_2 cell is rather low due to the low vertex potential applied (Figure S9b, Supporting Information) to hinder forming. In the thin oxide the defect formation rate is much higher owing to the high electric field, which in turn significantly lowers the forming voltage.

Hence, the different forming voltage and resistive switching ratio could be explained by the different oxygen reservoir capability of the Ti electrode. During the forming process, the oxygen ions are released from the hafnium oxide and diffuse toward Ti electrode driven by the electric field, accompanied by oxygen vacancy defect formation. A proper amount of Ti is needed for uptake the oxygen ions and form interfacial sub-stoichiometric oxide (Figure 7c). As the sweeping potential increases, more oxygen vacancies are generated and the filament grows toward HfO_2/TiN Schottky interface. This leads to decrease of Schottky barrier height and degrade the breakdown potential for the HfO_2. When utilizing a thin Ti layer, in this case 10 nm for 10 and 20 nm HfO_2 cells, the Ti is partially oxidized prior to device operation, thus the overall resistance of the cell increases, and higher voltage/energy is needed to induce the oxygen vacancy defects. In this case, the oxide breakdown potential (forming voltage) is also increased. High breakdown potential may result in accumulation of excessive oxygen vacancies (reduction) in the oxide (Figure 7d), making it difficult to reset the cell, and the resistive switching ratio is small (see Figure S10, Supporting Information). It is worth stressing that the selection of Ti thickness should be correlated with oxide thickness, i.e., the effective Ti thickness depends on the thickness of resistive switching layer. For instance, in this study, 10 nm Ti is difficult to lower the defect formation energy with respect to 10 nm HfO_2, whereas it is sufficient to take effect for that of 5 nm HfO_2. For a thin resistive switching layer, the defect density desired for reversible resistive switching is low in contrast to the thicker one. Hence, a lower amount of scavenging Ti is demanded for defect formation.

3. Conclusion

We have reported on the impact of the combination of electrode, electrolyte, capping layer materials and their thicknesses on the resistive switching behavior of HfO_2-based ECM and VCM devices. By conducting cyclic voltammetry and *I–V* measurement the redox processes and switching characteristics are studied. In ECM cells, we found the half-cell reaction at counter electrode is essential in sustaining redox reaction and resistive switching. The capping material is additional factor that influences metal ion concentration and diffusion coefficient in the oxide, thus influencing overall cell resistance and SET/RESET voltages. For VCM cells, we found active switching interface can be changed when employing different configurations of capping and bottom electrodes. During cell operation TiN is oxidized and can undergo oxygen ion exchange reaction, thus modifying the resistive switching behavior. For both types of cells, the thickness of oxide electrolyte and active (ohmic) electrode in combination needs to be carefully selected for obtaining reliable resistive switching.

The results highlight the general importance to consider all individual device components—electrodes, switching film and capping layer, and as well their thicknesses as an inherent materials combination for a reliable stack configuration. The results are obtained for HfO_2-based ECM and VCM devices, but due to the common electrochemical fundamental background, they are considered applicable for all type ReRAM memristive cells.

4. Experimental Section

Device Fabrication: The ReRAM devices investigated in this work were fabricated using standard optical lithography, metal deposition and lift-off processes. Firstly, a 5 nm titanium (Ti) adhesion layer and 30 nm platinum (Pt, or 30 nm TiN) bottom electrodes were deposited by direct current (DC) magnetron sputtering (power of 200 W) on thermally oxidized silicon substrate. The Pt and TiN electrodes serve as counter electrodes in ECM system and as Schottky electrode in VCM system. Afterward, hafnium dioxide (HfO_2) layer was deposited by radio frequency (RF) magnetron sputtering in Ar atmosphere from a pure ceramic HfO_2 target (99.95%). For ECM devices, the Cu (active electrode) layers were deposited by electron beam evaporation with an evaporation rate of 0.01 nm s^{-1}. For VCM devices, the Ti (ohmic electrode) layers were deposited by DC magnetron sputtering. The Pt and TiN capping layers were deposited by DC magnetron sputtering at same parameters as bottom electrodes. The TiN layers were reactively sputtered using a pure Ti (99.99%) metallic target under mixed Ar (27 sccm) and N_2 (3 sccm) atmosphere. The capping layers were deposited right after the formation of Cu or Ti electrodes without breaking the vacuum system. The ReRAM cells were structured by optical lithography. For calculation of Cu ion concentration in Figure 4, the cell geometry is considered to be the product of cell area (25×25 μm^2) times oxide thickness (10 nm).

Electrical Characterization: The cyclic voltammetry and current–voltage (*I–V*) sweep measurements were performed at ambient conditions (relative humidity ≈ 35%) using a Keithley 6430 Sub-FemtoAmp Remote SourceMeter connected to Cascade SUMMIT 9600 probe station. Triaxial measurement setup is employed in the measurement system, which allows measuring currents at the device between 0.01 pA and 105 mA with a sweep rate from 1 to 4 V s^{-1}. The vertex potentials are set to be smaller than the forming voltage during CV sweeping. For *I–V* measurements, current compliances (800 μA or 1 mA) were applied to prevent damage to the devices. Unless mentioned in the main text, in all the electrical measurements, the potentials were applied to the top electrodes of the devices, keeping the bottom electrodes grounded.

Supporting Information

Supporting Information is available from the Wiley Online Library or from the author.

Acknowledgements

The authors thank D. Erdoglija (IWE2, RWTH Aachen) for helping with sample preparation. C. Weber (Forschungszentrum Jülich) is acknowledged for the preparation of oxide targets. The work has been funded in part by the project (EMPIR 20FUN06 MEMQuD) that has received funding from the EMPIR programme cofinanced by the Participating States and from the European Union's Horizon 2020 research and innovation programme.

Open access funding enabled and organized by Projekt DEAL.

© 2021 The Authors. Advanced Materials published by Wiley-VCH GmbH

Conflict of Interest

The authors declare no conflict of interest.

Data Availability Statement

The data that support the findings of this study are available from the corresponding author upon reasonable request.

Keywords

capping layers, electrode materials, redox reactions, resistive switching, thicknesses

Received: June 30, 2021
Revised: October 19, 2021
Published online:

[1] Z. Wang, H. Wu, G. W. Burr, C. S. Hwang, K. L. Wang, Q. Xia, J. J. Yang, *Nat. Rev. Mater.* **2020**, *5*, 173.
[2] R. Aitken, V. Chandra, J. Myers, B. Sandhu, L. Shifren, G. Yeric, in *2014 Symp. on VLSI Technology (VLSI-Technology): Dig. Tech. Pap.*, IEEE, Piscataway, NJ, USA **2014**, https://doi.org/10.1109/VLSIT.2014.6894339
[3] G. W. Burr, *Nat. Mach. Intell.* **2019**, *1*, 10.
[4] Z. Wang, S. Joshi, S. Savel'ev, W. Song, R. Midya, Y. Li, M. Rao, P. Yan, S. Asapu, Y. Zhuo, H. Jiang, P. Lin, C. Li, J. H. Yoon, N. K. Upadhyay, J. Zhang, M. Hu, J. P. Strachan, M. Barnell, Q. Wu, H. Wu, R. S. Williams, Q. Xia, J. J. Yang, *Nat. Electron.* **2018**, *1*, 137.
[5] P. Yao, H. Wu, B. Gao, J. Tang, Q. Zhang, W. Zhang, J. J. Yang, H. Qian, *Nature* **2020**, *577*, 641.
[6] P. Lin, C. Li, Z. Wang, Y. Li, H. Jiang, W. Song, M. Rao, Y. Zhuo, N. K. Upadhyay, M. Barnell, Q. Wu, J. J. Yang, Q. Xia, *Nat. Electron.* **2020**, *3*, 225.
[7] G. C. Adam, B. D. Hoskins, M. Prezioso, F. Merrikh-Bayat, B. Chakrabarti, D. B. Strukov, *IEEE Trans. Electron Devices* **2017**, *64*, 312.
[8] D. Ielmini, H.-S. P. Wong, *Nat. Electron.* **2018**, *1*, 333.
[9] G. W. Burr, R. M. Shelby, A. Sebastian, S. Kim, S. Kim, S. Sidler, K. Virwani, M. Ishii, P. Narayanan, A. Fumarola, L. L. Sanches, I. Boybat, M. L. Gallo, K. Moon, J. Woo, H. Hwang, Y. Leblebici, *Adv. Phys.: X* **2017**, *2*, 89.
[10] K. Berggren, Q. Xia, K. K. Likharev, D. B. Strukov, H. Jiang, T. Mikolajick, D. Querlioz, M. Salinga, J. R. Erickson, S. Pi, F. Xiong, P. Lin, C. Li, Y. Chen, S. Xiong, B. D. Hoskins, M. W. Daniels, A. Madhavan, J. A. Liddle, J. J. McClelland, Y. Yang, J. Rupp, S. S. Nonnenmann, K.-T. Cheng, N. Gong, M. A. Lastras-Montaño, A. A. Talin, A. Salleo, B. J. Shastri, T. F. de Lima, P. Prucnal, A. N. Tait, Y. Shen, H. Meng, C. Roques-Carmes, Z. Cheng, H. Bhaskaran, D. Jariwala, H. Wang, J. M. Shainline, K. Segall, J. J. Yang, K. Roy, S. Datta, A. Raychowdhury, *Nanotechnology* **2020**, *32*, 012002.
[11] *Resistive Switching: From Fundamentals of Nanoionic Redox Processes to Memristive Device Applications* (Eds: D. Ielmini, R. Waser), Wiley-VCH, Weinheim, Germany **2016**.
[12] J. J. Yang, D. B. Strukov, D. R. Stewart, *Nat. Nanotechnol.* **2013**, *8*, 13.
[13] I. Valov, W. D. Lu, *Nanoscale* **2016**, *8*, 13828.
[14] I. Valov, E. Linn, S. Tappertzhofen, S. Schmelzer, J. van den Hurk, F. Lentz, R. Waser, *Nat. Commun.* **2013**, *4*, 1771.
[15] Q. Liu, J. Sun, H. Lv, S. Long, K. Yin, N. Wan, Y. Li, L. Sun, M. Liu, *Adv. Mater.* **2012**, *24*, 1844.
[16] I. Valov, R. Waser, J. R. Jameson, M. N. Kozicki, *Nanotechnology* **2011**, *22*, 254003.
[17] A. Wedig, M. Luebben, D.-Y. Cho, M. Moors, K. Skaja, V. Rana, T. Hasegawa, K. K. Adepalli, B. Yildiz, R. Waser, I. Valov, *Nat. Nanotechnol.* **2016**, *11*, 67.
[18] H. Yeon, P. Lin, C. Choi, S. H. Tan, Y. Park, D. Lee, J. Lee, F. Xu, B. Gao, H. Wu, H. Qian, Y. Nie, S. Kim, J. Kim, *Nat. Nanotechnol.* **2020**, *15*, 574.
[19] A. Mehonic, A. L. Shluger, D. Gao, I. Valov, E. Miranda, D. Ielmini, A. Bricalli, E. Ambrosi, C. Li, J. J. Yang, Q. Xia, A. J. Kenyon, *Adv. Mater.* **2018**, *30*, 1801187.
[20] S. Tappertzhofen, H. Mündelein, I. Valov, R. Waser, *Nanoscale* **2012**, *4*, 3040.
[21] A. Hardtdegen, C. La Torre, F. Cüppers, S. Menzel, R. Waser, S. Hoffmann-Eifert, *IEEE Trans. Electron Devices* **2018**, *65*, 3229.
[22] A. Marchewka, B. Roesgen, K. Skaja, H. Du, C.-L. Jia, J. Mayer, V. Rana, R. Waser, S. Menzel, *Adv. Electron. Mater.* **2016**, *2*, 1500233.
[23] S. Menzel, M. Waters, A. Marchewka, U. Böttger, R. Dittmann, R. Waser, *Adv. Funct. Mater.* **2011**, *21*, 4487.
[24] S. Tappertzhofen, I. Valov, T. Tsuruoka, T. Hasegawa, R. Waser, M. Aono, *ACS Nano* **2013**, *7*, 6396.
[25] M. Lübben, I. Valov, *Adv. Electron. Mater.* **2019**, *5*, 1800933.
[26] T. Tsuruoka, I. Valov, S. Tappertzhofen, J. van den Hurk, T. Hasegawa, R. Waser, M. Aono, *Adv. Funct. Mater.* **2015**, *25*, 6374.
[27] T. Tsuruoka, K. Terabe, T. Hasegawa, I. Valov, R. Waser, M. Aono, *Adv. Funct. Mater.* **2012**, *22*, 70.
[28] Z. Wang, S. Joshi, S. E. Savel'ev, H. Jiang, R. Midya, P. Lin, M. Hu, N. Ge, J. P. Strachan, Z. Li, Q. Wu, M. Barnell, G.-L. Li, H. L. Xin, R. S. Williams, Q. Xia, J. J. Yang, *Nat. Mater.* **2017**, *16*, 101.
[29] Y. Yang, P. Gao, S. Gaba, T. Chang, X. Pan, W. Lu, *Nat. Commun.* **2012**, *3*, 732.
[30] Q. Liu, S. Long, H. Lv, W. Wang, J. Niu, Z. Huo, J. Chen, M. Liu, *ACS Nano* **2010**, *4*, 6162.
[31] J. H. Yoon, J. Zhang, P. Lin, N. Upadhyay, P. Yan, Y. Liu, Q. Xia, J. J. Yang, *Adv. Mater.* **2020**, *32*, 1904599.
[32] C. Mannequin, T. Tsuruoka, T. Hasegawa, M. Aono, *Jpn. J. Appl. Phys.* **2016**, *55*, 06GG08.
[33] D. Cooper, C. Baeumer, N. Bernier, A. Marchewka, C. La Torre, R. E. Dunin-Borkowski, S. Menzel, R. Waser, R. Dittmann, *Adv. Mater.* **2017**, *29*, 1700212.
[34] M. Azzaz, E. Vianello, B. Sklenard, P. Blaise, A. Roule, C. Sabbione, S. Bernasconi, C. Charpin, C. Cagli, E. Jalaguier, S. Jeannot, S. Denorme, P. Candelier, M. Yu, L. Nistor, C. Fenouillet-Beranger, L. Perniola, in *2016 IEEE 8th Int. Memory Workshop (IMW)*, IEEE, Piscataway, NJ, USA **2016**, https://doi.org/10.1109/IMW.2016.7495268
[35] S. Wiefels, C. Bengel, N. Kopperberg, K. Zhang, R. Waser, S. Menzel, *IEEE Trans. Electron Devices* **2020**, *67*, 4208.
[36] Y. Guo, J. Robertson, *Appl. Phys. Lett.* **2014**, *105*, 223516.
[37] S. Wiefels, M. Von Witzleben, M. Huttemann, U. Bottger, R. Waser, S. Menzel, *IEEE Trans. Electron Devices* **2021**, *68*, 1024.
[38] M.-J. Lee, C. B. Lee, D. Lee, S. R. Lee, M. Chang, J. H. Hur, Y.-B. Kim, C.-J. Kim, D. H. Seo, S. Seo, U.-I. Chung, I.-K. Yoo, K. Kim, *Nat. Mater.* **2011**, *10*, 625.
[39] J. Woo, K. Moon, J. Song, S. Lee, M. Kwak, J. Park, H. Hwang, *IEEE Electron Device Lett.* **2016**, *37*, 994.
[40] A. J. Bard, R. Parsons, *Standard Potentials in Aqueous Solution*, 1st ed., M. Dekker, New York **1985**.
[41] M. Lübben, S. Menzel, S. G. Park, M. Yang, R. Waser, I. Valov, *Nanotechnology* **2017**, *28*, 135205.
[42] S. Tappertzhofen, R. Waser, I. Valov, *ChemElectroChem* **2014**, *1*, 1287.
[43] A. J. Bard, L. R. Faulkner, *Electrochemical Methods: Fundamentals and Applications*, John Wiley & Sons, Inc., New York **2001**.

© 2021 The Authors. Advanced Materials published by Wiley-VCH GmbH

[44] T. Tsuruoka, T. Hasegawa, I. Valov, R. Waser, M. Aono, *AIP Adv.* **2013**, *3*, 032114.
[45] T. Tsuruoka, I. Valov, C. Mannequin, T. Hasegawa, R. Waser, M. Aono, *Jpn. J. Appl. Phys.* **2016**, *55*, 06GJ09.
[46] D.-Y. Shih, C.-A. Chang, J. Paraszczak, S. Nunes, J. Cataldo, *J. Appl. Phys.* **1991**, *70*, 3052.
[47] C. Chang, *J. Appl. Phys.* **1982**, *53*, 7092.
[48] J. Chakraborty, U. Welzel, E. J. Mittemeijer, *J. Appl. Phys.* **2008**, *103*, 113512.
[49] D.-Y. Cho, S. Tappertzhofen, R. Waser, I. Valov, *Sci. Rep.* **2013**, *3*, 1169.
[50] M. Lübben, S. Wiefels, R. Waser, I. Valov, *Adv. Elect. Mater.* **2018**, *4*, 1700458.
[51] F. Borgatti, C. Park, A. Herpers, F. Offi, R. Egoavil, Y. Yamashita, A. Yang, M. Kobata, K. Kobayashi, J. Verbeeck, G. Panaccione, R. Dittmann, *Nanoscale* **2013**, *5*, 3954.
[52] A. Herpers, C. Lenser, C. Park, F. Offi, F. Borgatti, G. Panaccione, S. Menzel, R. Waser, R. Dittmann, *Adv. Mater.* **2014**, *26*, 2730.
[53] F. A. Kröger, *Chemistry of Imperfect Crystals: Imperfection Chemistry of Crystalline Solids*, 2nd ed., Elsevier Science Publishing Co Inc., Amsterdam, The Netherlands **1974**.
[54] W. C. Chien, Y. R. Chen, Y. C. Chen, A. T. H. Chuang, F. M. Lee, Y. Y. Lin, E. K. Lai, Y. H. Shih, K. Y. Hsieh, C.-Y. Lu, in *2010 Int. Electron Devices Meeting*, IEEE, Piscataway, NJ, USA **2010**, https://doi.org/10.1109/IEDM.2010.5703390.

© 2021 The Authors. Advanced Materials published by Wiley-VCH GmbH